DOI: 10.1002/ ((please add manuscript number))
Article type: Full paper

Ultrasmall $CuCo_2S_4$ Nanocrystals: All-in-One Theragnosis Nanoplatform with Magnetic Resonance/Near-Infrared Imaging for Efficiently Photothermal Therapy of Tumors

Bo Li, Fukang Yuan, Guanjie He, Xiaoyu Han, Xin Wang, Jinbao Qin, Zheng Xiao Guo, Xinwu Lu, Qian Wang, Ivan P. Parkin, Chengtie Wu**

Dr. B. Li, Mr F. K. Yuan, Mr. X. Wang, Dr. J. B. Qin, Prof. X. W. Lu
Department of Vascular Surgery, Shanghai Ninth People's Hospital, Shanghai JiaoTong University School of Medicine, Shanghai 200011, China.
E-mail: luxinwu@shsmu.edu.cn
Dr. B. Li, Prof. C. T. Wu
State Key Laboratory of High Performance Ceramics and Superfine Microstructure, Shanghai Institute of Ceramics, Chinese Academy of Sciences, Shanghai 200050, China.
E-mail:chengtiewu@mail.sic.ac.cn
Mr. F. K. Yuan
Department of Vascular Surgery, Xuzhou Central Hospital, Xuzhou 221009, Jiangsu, China.
Mr. G. J. He, Miss X. Y. Han, Prof. Z. X. Guo, Prof. I. P. Parkin
Christopher Ingold Laboratory, Department of Chemistry, University College London, London WC1H 0AJ, UK

Dr. Q. Wang

Department of Orthopaedics, Shanghai First People's Hospital, Shanghai Jiaotong University, Shanghai 200080, China.

Keywords: ternary bimetal chalcogenides, ultrasmall $CuCo_2S_4$ nanocrystals, DFT calculations, magnetic resonance imaging, photothermal therapy

Copper-based ternary bimetal chalcogenides have very promising potential as multifunctional theragnosis nanoplatform for photothermal treatment of tumors.

However, the design and synthesis of such an effective platform remains challenging. Herein, hydrophilic $CuCo_2S_4$ nanocrystals (NCs) with a desirable size of ~10 nm were synthesized by a simple one-pot hydrothermal route. The as-prepared ultrasmall $CuCo_2S_4$ NCs show: 1) intense near-infrared (NIR) absorption, which is attributed to 3*d*-electronic transitions from the valence band (VB) to an intermediate band (IB), as identified by Density Functional Theory (DFT) calculations; 2) high photothermal performance with a photothermal conversion efficiency up to 73.4%; and 3) capability for magnetic resonance (MR) imaging, as a result of the unpaired 3*d* electrons of cobalt. Finally, we, for the first time, demonstrated that the $CuCo_2S_4$ NCs are a promising "all-in-one" photothermal theragnosis nanoplatform for photothermal cancer therapy under the irradiation of a 915 nm laser at a safe power density of 0.5 W cm^{-2}, guided by MR and infrared thermal imaging. Our work further promotes the potential applications of ternary bimetal chalcogenides for photothermal theragnosis therapy.

1. Introduction

Copper-based chalcogenides have been proved as a new class of efficient photothermal therapy (PTT) agents due to their low cost, facile synthesis, high photothermal performance and good photostability, as well as their simple chemical formula with complicated crystal structures and variable compositions.[1, 2] Currently, several kinds of copper-based chalcogenides, such as Cu_9S_5,[3] Cu_9S_8,[4] $Cu_{7.2}S_4$,[5] $Cu_{2-x}Se$[6] and CuTe,[7] have been developed as PTT agents. These binary copper chalcogenides exhibit a strong absorption in near-infrared (NIR, 700-1400 nm) region that is frequently used by PTT agents and this results in deep penetration of the light to near surface tissue. The NIR absorption properties of copper-based chalcogenide nanostructures mainly result from 3*d* electron transition between Cu^{+} and Cu^{2+} in mixed valence materials, thus there is a coexistence of Cu^{+} and Cu^{2+} and even many copper vacancies in these copper-based chalcogenide nanostructures.[8, 9] Though considerable progresses have been achieved in the preparation of copper-based chalcogenide nanostructures, there still remains a notable challenge for copper-based chalcogenide nanostructures to be used in PTT, i.e. safety, the accumulation of nanoparticles in the vital organs without timely clearance from the body could lead to acute toxicity and/or a long-term inflammatory response. A direct and efficient strategy is to reduce the size of PTT agents to ≤ 10 nm that can be rapidly removed by the renal system, [10-13] decreasing the nanoparticles' accumulation in the vital organs. What's more, smaller PTT agents show better photothermal effect than larger ones due to less light scattering that does not contribute to heating when irradiated by lasers.[3, 6] However, smaller particles (≤ 10 nm) often have a drawback of shorter blood circulation time which doesn't benefit the tumor uptake of PTT agents. In addition, these copper-based chalcogenide nanostructures as PTT agents must be effective. For effective PTT, the agents should exhibit not only a high photothermal performance for **PTT** of cancers but a capacity of the diagnoses of cancers.[13-16] Therefore, it is of great importance to rationally design copper-based chalcogenides with small size, relatively long blood circulation time, high photothermal performance and imaging capability to realize efficient PTT of cancer.

It should be noted that most research on copper-based chalcogenides as PTT agents is copper-based binary chalcogenides ($Cu_{2-x}E$, E =S, Se, Te, $0 \leq x \leq 1$). Compared with binary chalcogenides, ternary bimetal chalcogenide nanomaterials could inherit the properties from their parent binary chalcogenides and produce new properties.[9, 17-19] However, only a few reports have been reported on these nanoscale copper-based ternary chalcogenides, due to the difficulty in synthesis of this type of nanomaterials as pure phases.[9, 20, 21] Our previous work on Cu_3BiS_3 nanocrystals (NCs) is the first report to demonstrate the feasibility of copper-based binary sulfides as a photothermal theragnosis agent.[9] These Cu_3BiS_3 NCs show a strong NIR absorption because of the coexistence of Cu^+ and Cu^{2+} and computed tomography (CT) imaging from the intrinsic property of bismuth, but unimpressive photothermal effect due to the size ~300 nm that results in more light scattering. The performances of Cu_3BiS_3 NCs have been greatly improved when the size is reduced to 10 nm,[13] However, a considerable high concentration (in the order of mg/mL range) of the PTT agents is required for the effective CT imaging,[13, 15, 22] which inevitably causes toxic effects to the body. In comparison with CT imaging, a relatively low concentration (in the order of ug/mL range) of the PTT agents is needed for effective magnetic resonance (MR) imaging.[20, 23-25] All in all, the synthesis of new ultrasmall copper-based ternary chalcogenide nanoparticles with strong NIR absorption and ability of MR imaging is highly desirable to meet the challenges in photothermal therapy.

Here, ultrasmall pure phase copper-based ternary chalcogenide nanoparticles,

$CuCo_2S_4$ NCs, are prepared by a one-pot hydrothermal route in the presence of ethylenediamine. The theoretical calculations reveal that there is an intermediate band (IB) in the fundamental gap of $CuCo_2S_4$, which leads to the as-prepared $CuCo_2S_4$ NCs exhibit strong NIR absorption resulted from the electron transitions from the valence band (VB) to the intermediate band (IB). The 915 nm-laser-irradiation of an aqueous suspension of $CuCo_2S_4$ NCs can exhibit significant heating, with a photothermal conversion efficiency of 73.4%. The as-prepared $CuCo_2S_4$ NCs also possess T_1-weighted magnetic resonance (MR) imaging because of unpaired 3d electrons of cobalt. Finally, we successfully demonstrated that the as-prepared ultrasmall $CuCo_2S_4$ NCs can be used as a novel and efficient "all-in-one" photothermal theragnosis agent for the MR/IR thermal imaging and photothermal therapy of cancers. To the best of our knowledge, the synthesis and bioapplication in photothermal theragnosis therapy of ultrasmall $CuCo_2S_4$ NCs have not yet been reported.

2. Results and Discussion

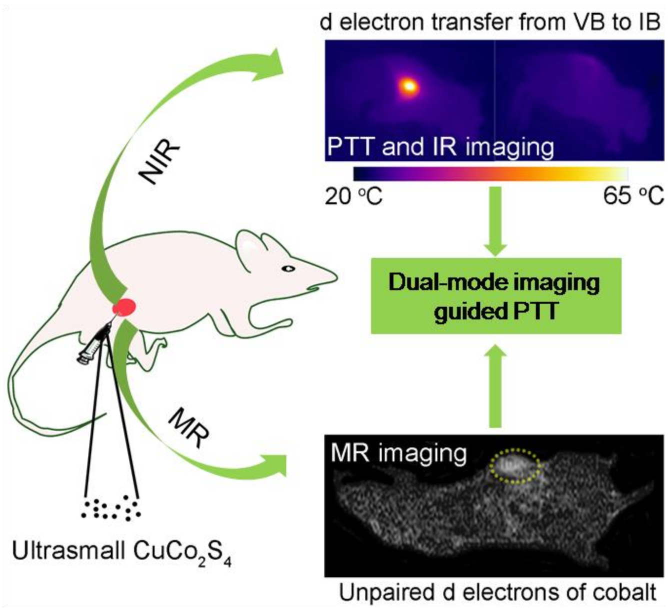

Scheme 1 . Schematic illustration of ultrasmall $CuCo_2S_4$ NCs used as a novel and efficient "all-in-one" photothermal theragnosis agent for the MR/IR thermal imaging and photothermal therapy of cancers.

As illustrated in **Scheme 1**, our "all-in-one" photothermal theragnosis nanoplatform are made from ultrasmall $CuCo_2S_4$ NCs. These nanocrystals were prepared by a facile one-pot hydrothermal synthesis method in the presence of ethylenediamine and poly vinyl pyrrolidone (PVP). Thus, ultrasmall $CuCo_2S_4$ NCs are hydrophilic and coated by PVP, evidenced by Fourier transform infrared spectrum (Figure S1). As a result, the NCs are hydrophilic without any modification, and they can remain unchanged after being dispersed in water for at least one month and in saline/ RPMI-1640 culture medium for 7 days (Figure S2) due to the small size and PVP coating. To confirm the crystallographic structure, the NCs were first measured by powder X-ray diffraction (XRD). As shown in **Figure 1**a, the pattern could be well indexed to the cubic spinel $CuCo_2S_4$ phase (JCPDS no. 42-1450). No peaks of any other phases were detected, indicating the high purity of the final product. More information on the composition and chemical bonding state of the NCs were performed by X-ray photoelectron spectroscopy (XPS, Figure S3 in the Supporting Information), showing that the as-prepared sample is mainly composed of Cu, Co, and S elements without other obvious impurities (the C and O peaks originate from the ligands). Figure 1b shows high-resolution XPS analysis of Cu 2p and Co 2p of $CuCo_2S_4$ NCs. The Cu 2p spectrum (red line) presented a $2p_{3/2}$ (931.8 eV) spin-orbit peak and a $2p_{1/2}$ (951.4 eV) spin-orbit peak; in addition, the Cu $2p_{3/2}$ satellite peak of Cu(II), which is usually located at about 942 eV, did not appear in the spectrum.[26] Therefore, there is only Cu(I) detected in $CuCo_2S_4$. Also, a Co $2p_{3/2}$ (778.1 eV) peak and a Co $2p_{1/2}$ (793.3 eV) peak, as well as two shakeup satellites, in the Co 2p spectrum (blue line) confirmed the coexistence of two cobalt oxidation state: Co^{2+} and Co^{3+}.[27] Based on the above results, it can be concluded that the pure $CuCo_2S_4$ phase was successfully formed.

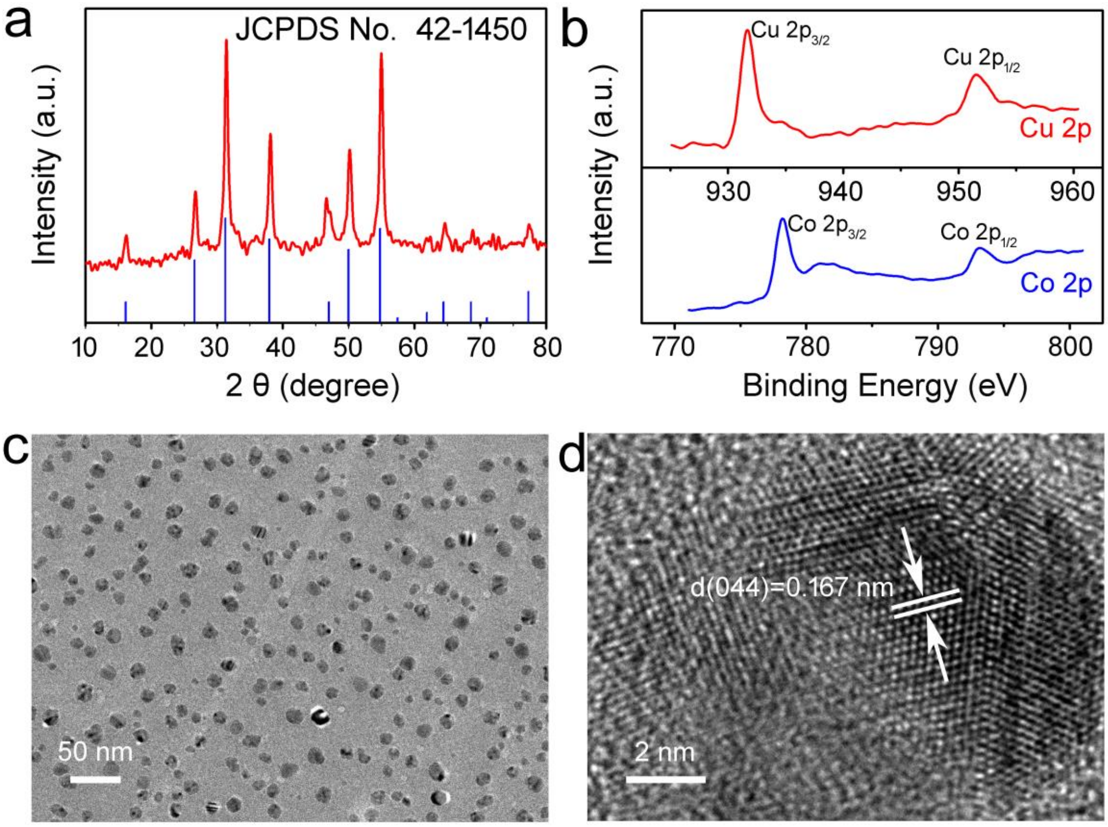

Figure 1. (a) Powder XRD patterns of the as-prepared nanocrystals (red line) and the standard $CuCo_2S_4$ powders (blue bar) from the JCPDS card (no. 42-1450). (b) high-resolution XPS spectra of Cu 2p and Co 2p. (c) Typical low-magnification and (d) HRTEM images of as-synthesized $CuCo_2S_4$ NCs.

The morphology and size of the as-synthesized $CuCo_2S_4$ NCs were measured by transmission electron microscopy (TEM). As shown in Figures 1c and S4, $CuCo_2S_4$

NCs are spherical particles with a size of 10±2 nm. Further investigation of the microstructure by high-resolution TEM (HRTEM) shows a well-defined crystalline lattice with an interplanar spacing of 0.167 nm (Figure 1d), which corresponds to the d-spacing for (044) planes of cubic spinel $CuCo_2S_4$ crystal. Nanomaterials prepared by hydrothermal system usually shows a size of above 100 nm,[2, 9, 28, 29] which have short circulation time as large nanoparticles could be removed by the reticuloendothelial system, primarily by the liver and spleen.[9, 30] The current as-prepared $CuCo_2S_4$ NCs, being only of 10±2 nm, may show longer blood circulation time when intravenously administered. This effective particle size reduction may be attributed to the presence of ethylenediamine, which acts as a complexing agents controlling the release rate of metal cations (Cu^{2+}, Co^{2+}) during the reaction. To clarify this, we also carried out the reaction without ethylenediamine, while keeping the other reaction conditions the same. As expected, the resulting $CuCo_2S_4$NCs are much larger, around 715±74 nm (Figure S5). Thus, the presence of ethylenediamine should be the main cause of forming the $CuCo_2S_4$ NCs with an ultrasmall size.

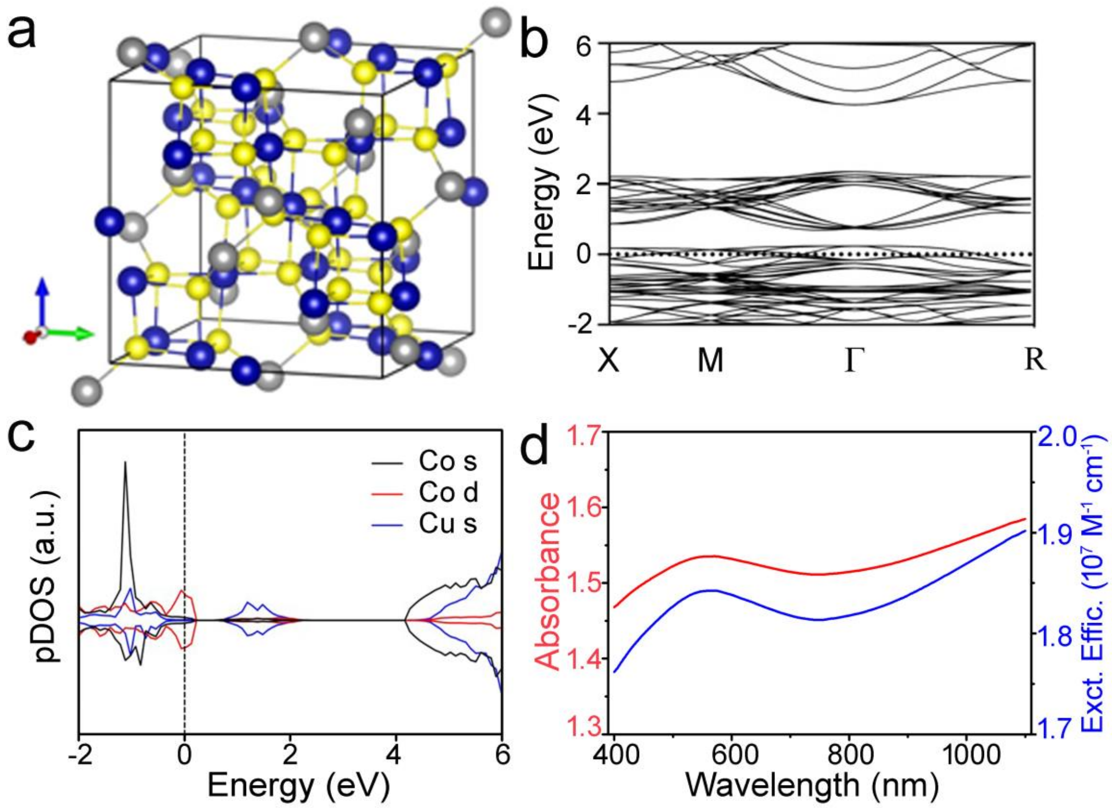

Figure 2. (a) The structure of the $CuCo_2S_4$, where the blue, grey and yellow ball represent Co, Cu, and S atoms, respectively. (b) Band structure of $CuCo_2S_4$. (c) Calculated projected Density of States (pDOS) of the $CuCo_2S_4$ of the major contributing orbitals by Co and Cu. (d) UV-vis absorbance spectrum (red line) and molar extinction coefficient (blue line) for the aqueous dispersion of the $CuCo_2S_4$ NCs.

The 3*d* electrons in the first-role of transition metals play an impotent role in the NIR absorption properties of the corresponding semiconductor compounds.[8, 31] In order to give the description of the highly correlated 3d electrons, Density Functional Theory with the on-site Coulomb interaction correction (DFT+U) approach was used to provide an accurate treatment of localised electron states, with U_{eff} set to 5 eV and 0.5

eV for Cu and Co, respectively, as well tested for the electronic structure and ground-state properties of Cu_2O and $FeCo_2S_4$[32, 33] The calculation details are given in the Supporting Information. The optimised structure is shown in **Figure 2**a, where the Co atoms are covalent bonding with S in an octahedral way, and the Cu are in a tetrahedral fashion with the S-Cu-S bond angle is 109.47^o. The calculated band structure and projected Density of States (pDOS) of $CuCo_2S_4$ NCs have been shown in Figure 2b&2c and Figure S6 in the Supporting Information, respectively. Clearly, the valence band (VB) maximum is located at Γ point, which is mainly contributed by the Co *d* orbital. On the other hand, the conduction band (CB) minimum is located along the Γ-R, which gives an indirect band gap of 0.47 eV. Notably, these lower CB, largely contributed by Cu atoms, gathered as a narrow intermediate band (IB) in the middle. This leaves a large empty band region apart from the higher conduction band with the bottom at Γ point, which corresponds to the secondary band gap of 2.12 eV. It should be noted that the indirect VB−IB gap of $CuCo_2S_4$ is narrower than that (0.67 eV) of $CuFeS_2$,[21] which means that optical absorption transition by electrons photoexcited to the IB is easier to realize, enhancing photoabsorption. As expected, the aqueous dispersion of $CuCo_2S_4$ NCs showed strong absorption from visible to NIR region, specially increased photoabsorption intensity from 750 to 1100 nm with a high molar extinction coefficient of ~ 1.8×10^7 M^{-1} cm^{-1} at 915 nm (Figure 2d), conferring the high NIR photothermal effect.

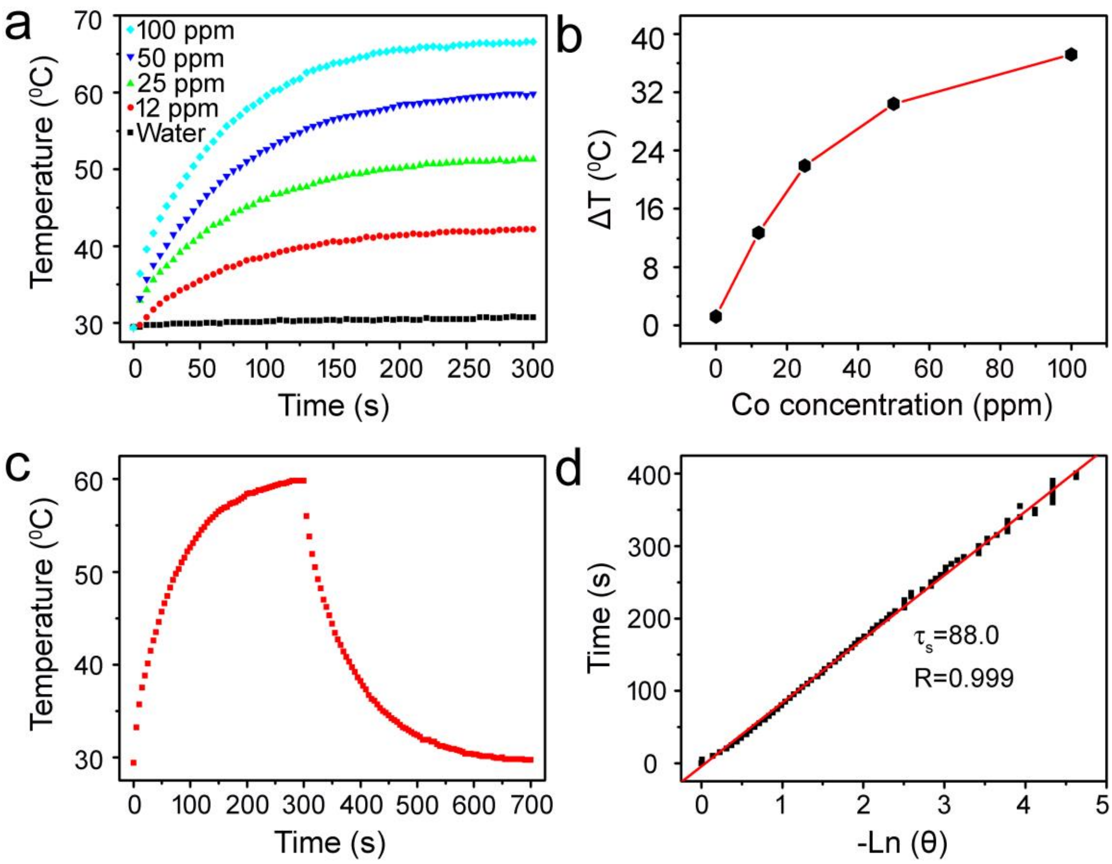

Figure 3. (a) Temperature elevation of the aqueous dispersion of $CuCo_2S_4$ NCs with different concentrations of Co^{2+} (i.e., 0, 12, 25, 50, and 100 ppm) under the irradiation of 915 nm laser with a power density of 0.5 W cm^{-2} as a function of irradiation time. (b) Plot of temperature change (ΔT) over a period of 300 s versus the aqueous dispersion concentration of cobalt NCs. (c) Photothermal effect of 50 ppm $CuCo_2S_4$ NCs upon being irradiated for 300 s (915 nm, 189 m W) and shutting off the laser. (d) Time constant for heat transfer from the system is determined to be τ_s = 88.0 s by applying the linear time data from the cooling period of panel (c) versus negative natural logarithm of driving force temperature.

Based on the features of different kinds of lasers and the NIR absorption of the $CuCo_2S_4$ NCs, a 915 nm laser was chosen to investigate the photothermal properties of NCs.[34] We first evaluated the photothermal performance of NCs at different concentrations (0-100 ppm) under the irritation of a 915 nm laser at a safe power density of 0.5 W cm^{-2} (**Figure 3**a&3b). Obviously, the $CuCo_2S_4$ NCs exhibited concentration-dependent photothermal effect, as a control, the temperature of pure water showed little change. It should be pointed out that the photothermal performance of $CuCo_2S_4$ NCs was noticeably better than that of our previously reported Cu_3BiS_3 NCs.[9] The temperature of a 0.26 mg/mL solution (100 ppm of cobalt, determined by ICP-AES) of $CuCo_2S_4$ NCs increased by 37.2 ^{o}C after irradiation of a 915 nm laser with a safe power density of 0.5 W cm^{-2}, while the temperature of 1 mg/mL of Cu_3BiS_3 NCs only increased by 15.3 ^{o}C after identical irradiation.

We then measured the photothermal conversion efficiency of $CuCo_2S_4$ NCs by a modified method similar to that on $Cu_{7.2}S_4$ NCs.[5] The photothermal conversion efficiency, η_T , was calculated using the following Eq. 1:

$$\eta_T = \frac{\mathrm{hA}(\mathrm{T}_{\max} - \mathrm{T}_{amb}) - Q_0}{I(1-10^{-A_\lambda})} \qquad (1)$$

Where h is the heat transfer coefficient, A is the surface area of the container. T_{max} is the maximum system temperature, T_{amb} is the ambient surrounding temperature and (T_{max} - T_{amb}) was 30.7 ^{o}C according to Figure 3c. *I* is the laser power (in units of mW, 189 mW) and A_λ is the absorbance (1.5351) at the excitation wavelength of 915 nm. Q_0 is the heat input (in units of mW) due to light absorption by the solvent. The lumped quantity hA was determined by measuring the rate of temperature drop after removing the light source. The value of hA is derived according to Eq. 2:

$$\tau_s = \frac{m_D C_D}{hA} \qquad (2)$$

where τ_s (88.0 s) is the sample system time constant, m_D and C_D are the mass (0.1 g) and heat capacity (4.2 J g^{-1}) of deionized water used as solvent, respectively. The Q_0 was measured independently and found to be 11.76 mW. Thus, the 915 nm laser heat conversion efficiency of $CuCo_2S_4$ NCs can be calculated to be 73.4% which is much higher than those of other copper chalcogenides.[3, 5, 6] For comparison, we also measured the photothermal conversion efficiency of the 715 nm $CuCo_2S_4$ nanostructures obtained from the reaction without ethylenediamine. Figure S7 illustrates the measured photothermal conversion efficiency of larger $CuCo_2S_4$ nanostructures, to be 57.4%, much lower than that of 10 nm $CuCo_2S_4$ NCs, due to the fact that lager nanostructures show more light scattering that does not contribute to heating when the photothermal agents are irradiated by lasers.[6]

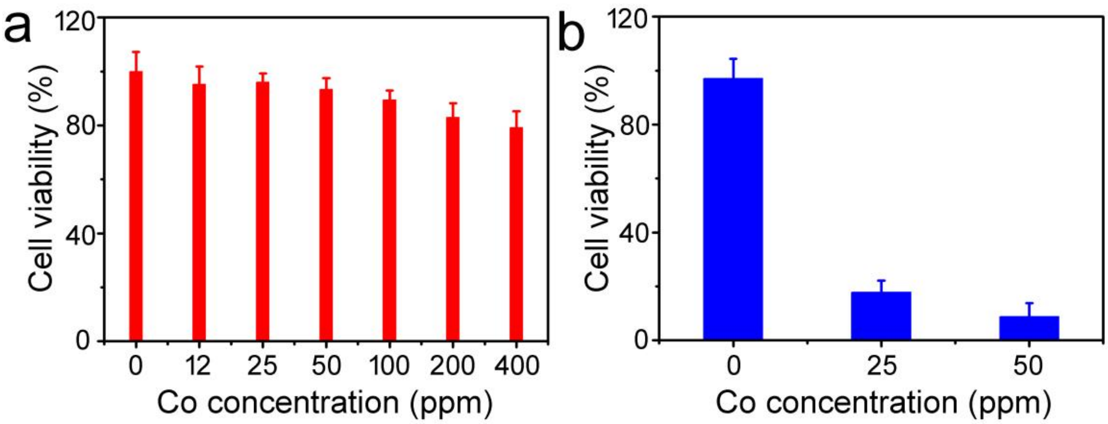

Figure 4. (a) The TC71 cell viability incubated with the $CuCo_2S_4$ NCs with different concentrations for 24 h. (b) Cell viability after treatment with different concentrations of the $CuCo_2S_4$ NCs under a 915 nm laser irradiation at a safe power density of 0.5 W cm^{-2}.

Such remarkable photothermal conversion performance of $CuCo_2S_4$ NCs motivated us to utilize these NCs as excellent photothermal agents. Prior to realization of their bioapplication, CCK8 assay with TC71 cells was used to evaluate the cytotoxicity of $CuCo_2S_4$ NCs. As expected, the results in **Figure 4**a show almost no cytotoxicity to TC71 cells for $CuCo_2S_4$ NCs with cobalt concentrations below 200 ppm, with the cell viability remaining at around 80% when the cobalt concentration was increased to 400 ppm. We also investigated the long-term toxicity in vivo of these $CuCo_2S_4$ NCs by histological examination (H&E) analysis for the major organs from the treated mice by a single intravenous NCs (400 ppm, 100 μL) or PBS solution (100 μL) injection, respectively. There is no appreciable tissue damage or adverse effect for mice 30 days after the administration of the $CuCo_2S_4$ NCs (Figure S8). Based on the excellent biocompatibility of $CuCo_2S_4$ NCs, the photothermal cytotoxicity of the $CuCo_2S_4$ NCs in different concentrations was evaluated with a 915 nm laser at 0.5 W cm^{-2}. After treatment, CCK8 assay was then used to evaluate the photothermal cytotoxicity, as shown in Figure 4b. TC71 cells could not be killed when treated only with $CuCo_2S_4$ NCs or by laser irradiation. However, they could be efficient killed with increasing nanocrystals concentration when treated with a combination of $CuCo_2S_4$ NCs and laser irradiation.

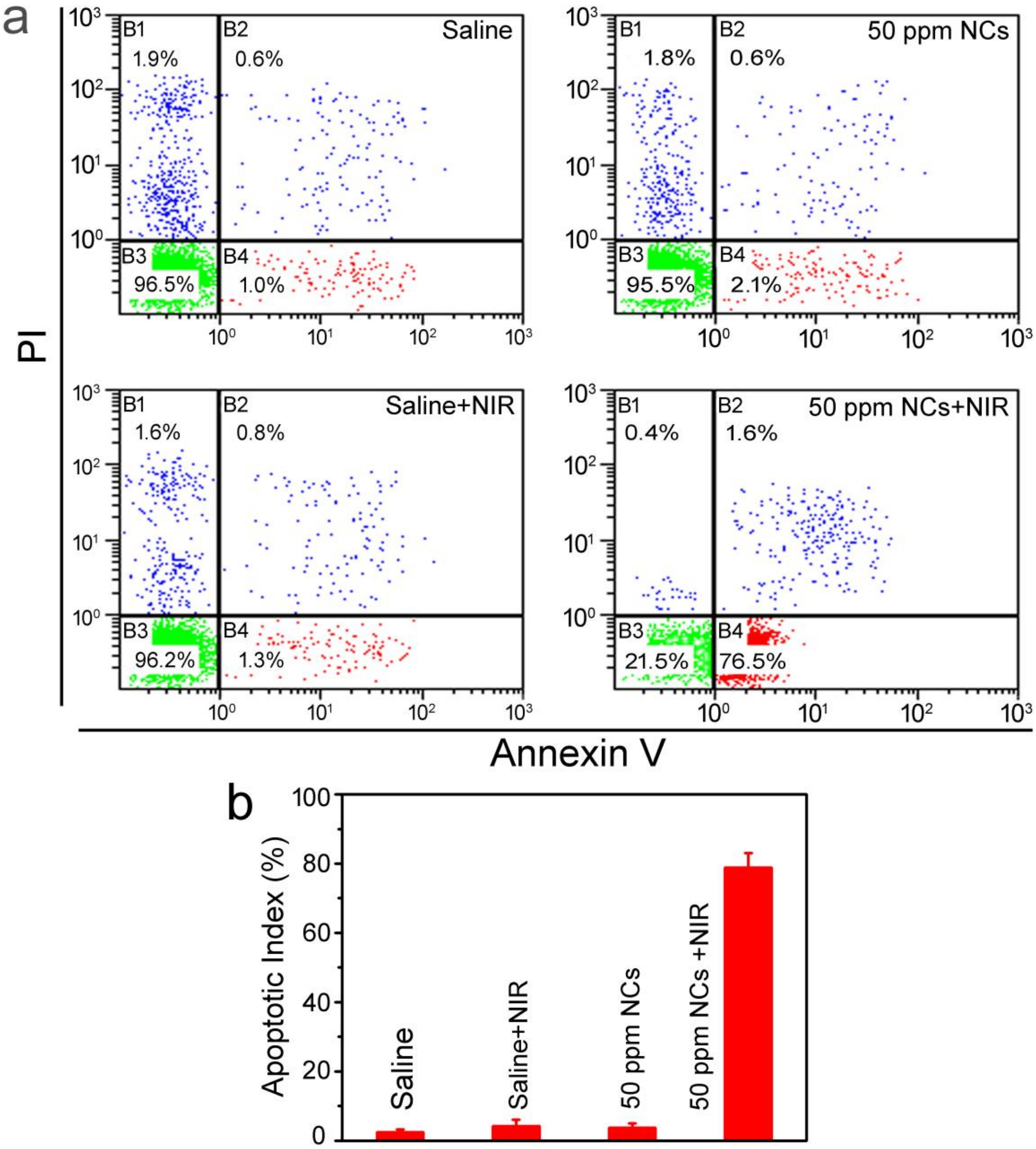

Figure 5. (a) Flow cytometry analysis of cancer cell apoptosis after the indicated treatment. (b) Apoptotic index from panel (a).

The treated TC71 cells were also incubated with Annexin V/PI and analyzed by flow cytometry to investigate the cytotoxicity of the $CuCo_2S_4$ NCs (**Figure 5**a). The results were in accordance with those of CCK8 assay. Compared to the three control groups, significantly higher apoptosis (78.89 $\pm$ 4.15%) could be observed in TC71 cells treated together with the $CuCo_2S_4$ NCs or laser irradiation (Figure 5b). These results demonstrated that TC71 cells can be efficient killed due to the remarkable photothermal conversion performance of $CuCo_2S_4$ NCs.

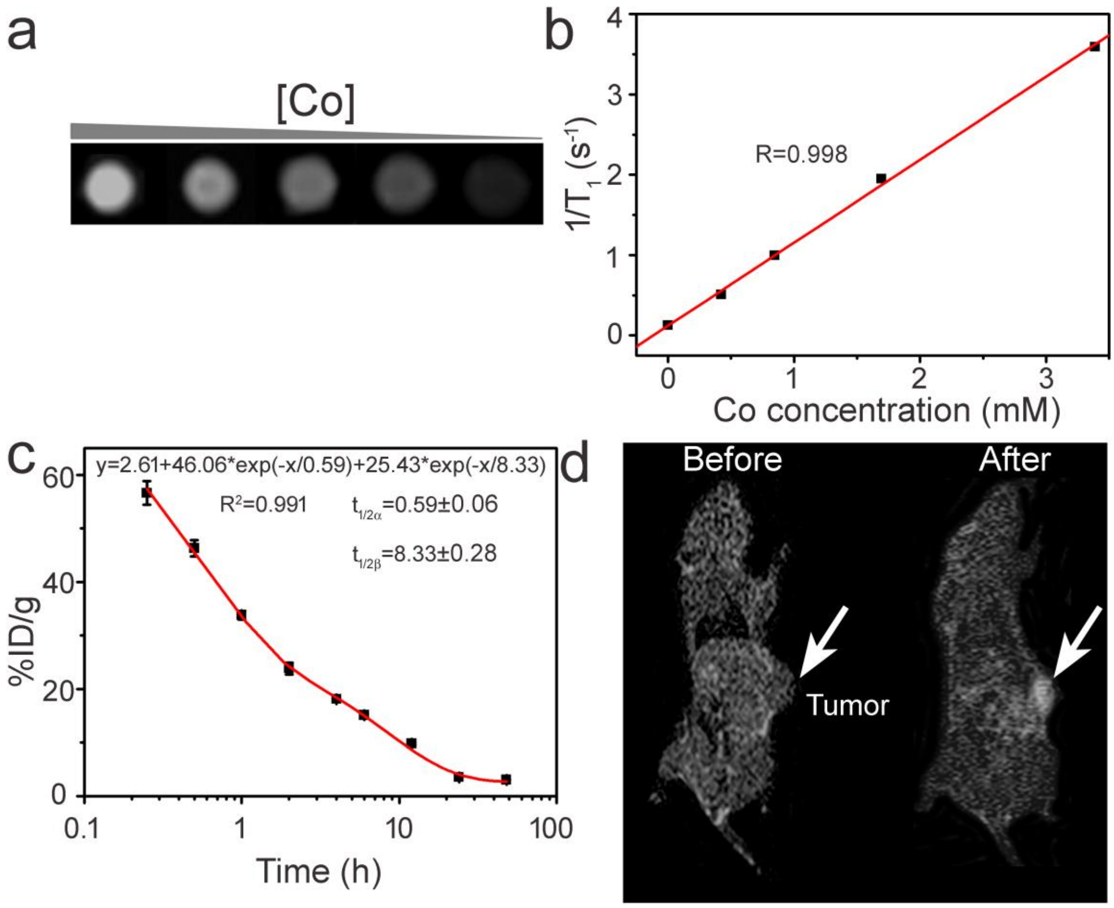

Figure 6. (a) In vitro T_1-weighted MR images of the $CuCo_2S_4$ NCs with different aqueous dispersion concentrations. (b) Plots of the $1/T_1$ value of the $CuCo_2S_4$ NCs as a function of the concentration of NCs. (c) blood circulation of $CuCo_2S_4$ NCs following an intravenous injection into tumor-bearing mice, as determined by measuring Co concentrations in tissue lysates with ICP-AES. (d) In vivo T_1-weighted MR coronal views of a mouse before and after an intratumoral injection of the solution of the $CuCo_2S_4$ NCs.

In addition to the issue of the photothermal therapy, $CuCo_2S_4$ NCs could be used for diagnoses. Previous reports have demonstrated that metal iron with unpaired electrons, such as Cu(II), Mn(II) and Gd (III), can be a candidates for T_1-weighted magnetic resonance (MR) imaging contrast agent.[35-37] In the as-prepared $CuCo_2S_4$ NCs, Co^{2+} and Co^{3+} also normally possess unpaired 3*d* electrons (Figure 1b). Thus, as-prepared $CuCo_2S_4$ NCs may have a great potential to be MR imaging contrast agents. To verify our hypothesis, phantom images of aqueous dispersions of the $CuCo_2S_4$ NCs and proton T_1 relaxation measurements at varied Co concentration were performed under a 3T MR clinical scanner. Encouragingly, the T_1-weighted MR images of the $CuCo_2S_4$ NCs showed a concentration-dependent brightening effect (**Figure 6**a). The corresponding longitudinal relaxivity (**r_1**) of the $CuCo_2S_4$ NCs was calculated to be **r_1**=1.02 mM^{-1} s^{-1}, obtained from the slope of the reciprocal of T_1 (**r_1** =1/T_1) at various Co concentrations (Figure 6b). The **r_1** value is lower than that of Mn(II)-based nanoparticles,[23] but higher than that of Cu(II)-based nanoparticles.[25] The short blood circulation time of imaging contrast agents will limit their applications to target imaging. Before the ultrasmall $CuCo_2S_4$ NCs were used as in vivo MR imaging agents, they were intravenously injected into healthy nude mice to measure the blood circulation time of $CuCo_2S_4$ NCs. Then collected blood samples at different time points were digested with HNO_3/H_2O_2 solution to determine their cobalt contents by ICP-AES measurements. As shown in Figure 6c, $CuCo_2S_4$ NCs exhibit a relatively long blood circulation with a half-life of 8.33 h. Then, the contrast enhancing effect in vivo was evaluated in TC71 tumor-bearing nude mice before and after intratumoral injection of the ultrasmall $CuCo_2S_4$ NCs dispersed in a saline solution (100 μL, 200 ppm). As shown in Figure 6d, T_1-weighted MR signal showed up in the tumor after injection of $CuCo_2S_4$ NCs, exhibiting a brighter contrast than other soft tissues. Thus, the as-prepared ultrasmall $CuCo_2S_4$ NCs are a kind of promising MR imaging agents due to their relatively high longitudinal relaxivity and long blood circulation time.

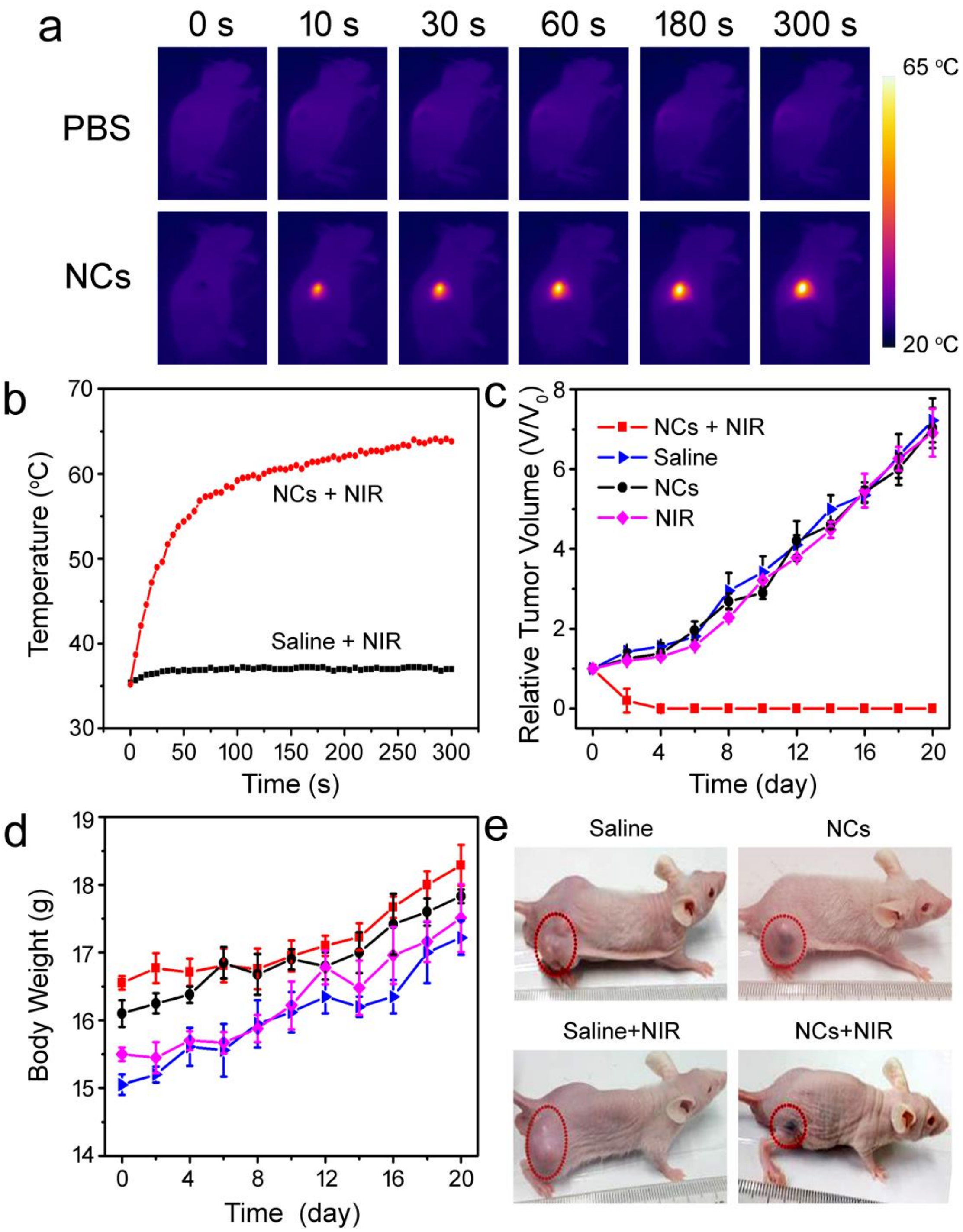

Figure 7. (a) Infrared thermal imaging of tumor-bearing mice after an intratumoral injection of saline or NCs and exposure to 915 nm laser irradiation at a safe power density of 0.5 W cm^{-2}. (b) Temperature change curves of tumors in mice from (a) as a function of irradiation time. (c) Growth curves of tumors in mice from the different treatment groups. Tumor volumes were normalized to their initial sizes. Error bars represent the standard deviations of 5 mice per group. (d) Body weight curves of mice in the different treatment groups. (e) Representative photos of mice in different groups at the 10th day after PTT treatment.

The excellent PTT in vitro of as-prepared ultrasmall $CuCo_2S_4$ NCs motivated us to evaluate the PTT of cancer cells in vivo under the guidance of infrared thermal imaging. When the tumors in the 24 mice were allowed to grow to a size of 5-10 mm in diameter, the mice were randomly divided into four groups with six mice per group and then treated differently. The four groups are referred to as (a) mice injected with a $CuCo_2S_4$ NC solution dispersed in saline and then irradiated for 5 min by a 915 nm laser at a safe power density of 0.5 W cm^{-2} (Group 1, $CuCo_2S_4$ NCs + NIR); (b) mice injected with a saline solution and then irradiated by the same 915 nm laser (Group 2, PBS + NIR); (c) mice injected with a PBS solution only(Group 3, PBS); and (d) mice injected with a $CuCo_2S_4$ NC solution dispersed in saline only (Group 4, $CuCo_2S_4$ NCs). The full-body infrared thermal images and the temperature change of the tumor area under NIR irradiation were monitored by an infrared thermal camera. As shown in **Figure 7**a, infrared thermal images with remarkable contrast could be achieved.

For the NCs' solution injected-mice (100 μL, 50 ppm), the tumor surface temperatures increased dramatically from ~35 °C to ~63 °C during the 5 min irradiation process, which is sufficient to denature the cancer cells (Figure 7b). In contrast, the surface temperature of the tumor area of the mice injected with a saline solution (100 μL) increased by less than 2 °C under the same irradiation condition. These results indicate that the $CuCo_2S_4$ NCs still possess an excellent photothermal effect in vivo.

The tumor sizes and body weights of mice were measured every 2 days after the above indicated treatments. Figure 7c exhibits the tumor volume change of mice from the treated four groups as a function of time. It was found that the tumors in three control groups, including PBS injection with (Group 2) or without laser irradiation (Group 3), and $CuCo_2S_4$ NC injection without laser irradiation (Group 4), showed rapid but indistinguishable growth rates. In marked contrast, the tumors treated by laser irradiation with the aid of $CuCo_2S_4$ NCs (Group 1) shrank and became black scars at day 2, and were completely eliminated in 10 days (Figure 7e). No reoccurrence was observed in the following days (Figure 7c). Additionally, it was observed that the body weights of mice in the four groups were not significantly affected after receiving indicated treatments (Figure 7d), suggesting that the current dose of ultrasmall $CuCo_2S_4$ NCs/915 nm-laser irradiation did not induce acute toxicity or noticeable toxic and side effects. Hematoxylin and eosin (H&E) staining of the tumors slices was also performed immediately after treatments. Cancer cells in control groups (Group 2-4) mainly retained their normal size and morphology, while typical signs of cell damage, such as nuclear necrosis and karyopyknosis, were noticed in the tumors with both NC injection and laser irradiation (Figure S9). These results are in good agreement with the tumor growth data, further confirmed the highly effective and feasible therapeutic efficacy of the combination of ultrasmall $CuCo_2S_4$ NCs and irradiation of a 915 nm laser with a safe power density.

3. Conclusions

In summary, the introduction of ethylenediamine into a hydrothermal synthesis enables the production of hydrophilic $CuCo_2S_4$ NCs with a desirable small average size of 10 nm. The presence of an IB in the electronic band structure in $CuCo_2S_4$ NCs (as supported by DFT+U calculations) accounts for why these NCs absorb intensively the NIR radiation, due to ready electron transfer from the VB to the IB. The as-prepared $CuCo_2S_4$ NCs exhibit a highly photothermal conversion efficiency up to 73.4% due to intense NIR absorption, relatively small indirect VB-IB gap (0.45 eV) and small size. Also, these $CuCo_2S_4$ NCs show an effective MR imaging response derived from the unpaired 3*d* electrons, particularly enriched by Co. Furthermore, cancer cells in vitro and in vivo can be efficiently killed by the photothermal effects of NCs under the irradiation of 915 nm laser at a comparable safe density of 0.5 W cm^{-2}. Therefore, ultrasmall $CuCo_2S_4$ NCs have a great superiority as a novel "all-in-one" photothermal theragnosis agent due to high photothermal conversion efficiency, MR imaging response, long blood circulation time as well as their low cytotoxicity and low cost. Further studies on targeted cancer therapy and distribution in vivo are underway.

4. Experimental Section

Synthesis of ultrasmall $CuCo_2S_4$ nanocrystals. All the reagents were purchased from Sinopharm Chemical Reagent Co., Ltd. (Shanghai, China) and used without further purification. $CuCl_2$•$2H_2O$ (0.25 mmol), $CoCl_2$•$6H_2O$ (0.5 mmol), thiourea (1.5 mmol) and poly (vinyl pyrrolidone) (PVP, K30) were mixed together and dissolved in 30 mL deionized (DI) water under vigorously magnetic stirring. Then, 100 μL ethylenediamine was slowly added into the above solution. Finally, the resulting solution was transferred to a stainless steel autoclave, sealed, and heated at 160 ^{o}C for 20 h. A black precipitate was collected by centrifugation and washed with ethanol and deionized water several times.

Instrumentation and Characterization. The morphology, size, and microstructure of $CuCo_2S_4$ NCs were determined by a transmission electron microscope (JEM-2010F; Japan). XRD measurements were performed on a D/max-2550 PC X-ray diffractometer (XRD; Rigaku, Japan). UV-vis absorbance spectra and diffuse reflectance spectra were measured at room temperature using a UV-visible-NIR spectrophotometer operating from 400 to 1100 nm (Shimadzu UV-3600; Japan). XPS measurements were performed on an X-ray photoelectron spectroscopy (XPS; ESCALab250; USA). Contents of irons released from as-synthesized $CuCo_2S_4$ NCs in the samples were determined by an inductively coupled plasma atomic emission spectroscopy (ICP-AES; Prodigy; USA). FTIR spectra were measured from the samples in KBr pellets using a Fourier transform infrared spectrometer (FTIR; Nicolet

6700; USA). The 915 nm semiconductor lasers were purchased from Shanghai Xilong Optoelectronics Technology Co. Ltd., China, whose power could be adjusted externally (0-2 W). The output power of lasers was independently calibrated using a hand-held optical power meter (Newport model 1918-C, CA, USA).

To measure the photothermal performance, the solution (100 μL) of $CuCo_2S_4$ NCs with various concentrations were irradiated by the 915 nm semiconductor laser devices at a safe power density of 0.5 W cm^{-2} (~ 189 mW for a spot size of ~ 0.38 cm^2) for 5 min. The temperature was monitored and imaged simultaneously by a thermal imaging camera (FLIR A300, USA).

Theoretical calculations. First-principle spin-polarized calculations were carried out using the PBE functional for the exchange-correlation approximation, implanted in the Vienna *Ab initio* Simulation Package(VASP).[38, 39] The lattice parameter is adopted from experimental data, 9.4504Å.[40] A plane wave cutoff of 350 eV was selected, witha projector-augment wave (PAW) pseudopotential to treat the core electrons.[41] All atoms were fully relaxed until the change in force upon ionic displacement was less than 0.01 eV/Å, with the change in energies no greater than 10^{-5} eV. A Gamma-centered Monkhorst-Pack grid of 7*7*7 k-points was used for all the calculations.[42, 43]

In order to improve the description of the highly correlated *3d* electrons, the rotational invariant form, DFT+U approach, was used to provide an accurate treatment of localised electron states, with U_{eff} set to 5 eV and 0.5 eV for Cu and Co, respectively. They have shown to reproduce well the electronic structure and ground-state properties of Cu_2O and $FeCo_2S_4$.[32, 33] In order to driven electron localization to either Cu^+, Co^{2+} or Co^{3+} state, the initial magnetic moments on Cu and Co atoms are set.

In vitro cell viability assay. The in vitro cytotoxicity was evaluated using the Cell Counting Kit-8 (CCK-8) (Dojindo Laboratories, Kumamoto, Japan). TC71 cells were seeded into a 96-plate, and incubated with the NCs at different concentrations , and then followed either with or without 915 nm NIR laser irradiation at a safe power density of 0.5 W cm^{-2} for 5 min. Finally, cell viabilities were then detected using the CCK-8 assay. Moreover, cells processed as above were also determined by flow cytometry after Annexin V/PI (eBioscience, San Diego, USA) staining. The washing process with phosphate buffer solution (PBS) was performed in all experiments after incubation with NCs. All experiments were independently performed three times.

MR Imaging. The $CuCo_2S_4$ NCs with various concentrations (0-3.39 mM) was scanned under a 3 T clinical MRI scanner at room temperature. The relaxation rate r_1 was calculated as the reciprocal of T1 (γ_1 =1/T1) at various cobalt concentrations. For in vivo MR imaging, TC71 tumor-bearing nude mice were intratumorally injected with $CuCo_2S_4$ NCs (100 μL, 400 ppm) when the tumor size reached to 5-10 mm. Small animal MR images were collected and analyzed on a 3 T clinical MRI scanner equipped with a special animal imaging coil. All animal experiments were performed in accordance with the guidelines of the Institutional Animal Care and Use Committee.

In vivo Photothermal Ablation. The TC71 tumor-bearing nude mice were intratumorally injected with of the $CuCo_2S_4$ NCs' solution (100 μL, 50 ppm) or saline solution. After 0.5 h post-injection, the mice with or without the $CuCo_2S_4$ NCs' injection were simultaneously irradiated with the 915 nm laser at a safe power density of 0.5 W cm^2 power density for 5 min. During the laser irradiation, full-body infrared thermal images were captured using an IR camera from a photothermal therapy monitoring system (FLIR A300, USA). The tumor sizes and the weight of body were measured every 2 days. The tumor sizes calculated following the volume = (tumor length) × (tumor width)^2/2. Relative tumor volumes were calculated as V/V_0 (V_0 is the tumor volume when the treatment was initiated). For histological examination of the tumors, a mouse from each group were sacrificed after indicated treatment, and tumors were harvested, embedded in paraffin, and cryosectioned into 4 μm slices using a conventional microtome. The slices were stained with hematoxylin/eosin and examined under a Zeiss Axiovert 40 CFL inverted fluorescence microscope. The images were captured with a Zeiss AxioCam MRc5 digital camera.

Histological Examination Analysis. Tumor-bearing mice were intravenously injected with NCs dispersed in PBS solution (100 μL, 400 ppm). For the control, mice were intravenously injected with 100 μL of saline solution. After one month post-injection, major organs from both treatment and control groups were harvested, including the heart, lung, liver, spleen, intestine, and kidney. Then histological examination of organs was performed by means of microscopic imaging.

Blood circulation. For blood circulation time of $CuCo_2S_4$ NCs, blood samples were collected from the each mouse at the indicated time points, weighed, and then digested with HNO_3/H_2O_2 solution to analyze the total amount of cobalt in the blood using ICP-AES.

Supporting Information

Supporting Information is available online from the Wiley Online Library or from the author.

Acknowledgements

B. Li, F. K. Yuan and G. J. He contributed equally to this work. The authors acknowledge our membership of the UK's HPC Materials Chemistry Consortium, which is funded by Engineering and Physical Sciences Research Council (EP/L000202). The authors would thank the use of the UCL Legion High Performance Computing Facility and associated support services, in the completion of this work. The authors also appreciate the support by the National Key Research and Development Program of China (2016YFB0700803), Natural Science Foundation of China (Grant 81472048, 81370423), Key Research Program of Frontier Sciences, CAS (QYZDB-SSW-SYS027) and Program of Shanghai Outstanding Academic Leaders (15XD1503900), Natural Science Foundation of Jiangsu Province, China (BK20161168).

Received: ((will be filled in by the editorial staff))

Revised: ((will be filled in by the editorial staff))

Published online: ((will be filled in by the editorial staff))

References

[1] J. M. Luther, P. K. Jain, T. Ewers, A. P. Alivisatos, *Nat. Mater.* **2011**, *10*, 361.

[2] Q. Tian, M. Tang, Y. Sun, R. Zou, Z. Chen, M. Zhu, S. Yang, J. Wang, J. Wang, J. Hu, *Adv. Mater.* **2011**, *23*, 3542.

[3] Q. Tian, F. Jiang, R. Zou, Q. Liu, Z. Chen, M. Zhu, S. Yang, J. Wang, J. Wang, J. Hu, *ACS Nano* **2011**, *5*, 9761.

[4] Q. Tian, J. Hu, Y. Zhu, R. Zou, Z. Chen, S. Yang, R. Li, Q. Su, Y. Han, X. Liu, *J. Am. Chem. Soc.* **2013**, *135*, 8571.

[5] B. Li, Q. Wang, R. Zou, X. Liu, K. Xu, W. Li, J. Hu, *Nanoscale* **2014**, *6*, 3274.

[6] C. M. Hessel, V. P. Pattani, M. Rasch, M. G. Panthani, B. Koo, J. W. Tunnell, B. A. Korgel, *Nano Lett.* **2011**, *11*, 2560.

[7] W. Li, R. Zamani, P. Rivera Gil, B. Pelaz, M. Ibanez, D. Cadavid, A. Shavel, R. A. Alvarez-Puebla, W. J. Parak, J. Arbiol, A. Cabot,. *J. Am. Chem. Soc.* **2013**, *135*, 7098.

[8] Y. Li, W. Lu, Q. Huang, M. Huang, C. Li, W. Chen, *Nanomedicine* **2010**, *5*, 1161.

[9] B. Li, K. Ye, Y. Zhang, J. Qin, R. Zou, K. Xu, X. Huang, Z. Xiao, W. Zhang, X. Lu, J. Hu, *Adv. Mater.* **2015**, *27*, 1339.

[10] H. S. Choi, W. Liu, P. Misra, E. Tanaka, J. P. Zimmer, B. Itty Ipe, M. G. Bawendi, J. V. Frangioni, *Nat. Biotechnol.* **2007**, *25*, 1165.

[11] H. S. Choi, B. I. Ipe, P. Misra, J. H. Lee, M. G. Bawendi, J. V. Frangioni, *Nano Lett.* **2009**, *9*, 2354.

[12] F. Osaki, T. Kanamori, S. Sando, T. Sera, Y. Aoyama, *J. Am. Chem. Soc.* **2004**, *126*, 6520.

[13] J. Liu, P. Wang, X. Zhang, L. Wang, D. Wang, Z. Gu, J. Tang, M. Guo, M. Cao, H. Zhou, Y. Liu, C. Chen, *ACS Nano* **2016**, *10*, 4587.

[14] J. Yu, Y. Ju, L. Zhao, X. Chu, W. Yang, Y. Tian, F. Sheng, J. Lin, F. Liu, Y. Dong, Y. Hou, *ACS nano* **2016**, *10*, 159.

[15] J. Yu, C. Yang, J. Li, Y. Ding, L. Zhang, M. Z. Yousaf, J. Lin, R. Pang, L. Wei, L. Xu, F. Sheng, C. Li, G. Li, L. Zhao, Y. Hou, *Adv. Mater.* **2014**, *26*, 4114.

[16] D. E. Lee, H. Koo, I. C. Sun, J. H. Ryu, K. Kim, I. C. Kwon, *Chem. Soc. Rev.* **2012**, *41*, 2656.

[17] X. Gou, F. Cheng, Y. Shi, L. Zhang, S. Peng, J. Chen, P. Shen, *J. Am. Chem. Soc.* **2006**, *128*, 7222.

[18] Z. Bai, W. Ji, D. Han, L. Chen, B. Chen, H. Shen, B. Zou, H. Zhong, *Chem. Mater.* **2016**, *28*, 1085.

[19] H. Zhong, Z. Bai, B. Zou, *J. Phys. Chem. Lett.* **2012**, *3*, 3167.

[20] Q. Zhao, X. Yi, M. Li, X. Zhong, Q. Shi, K. Yang, *Nanoscale* **2016**, *8*, 13368.

[21] S. Ghosh, T. Avellini, A. Petrelli, I. Kriegel, R. Gaspari, G. Almeida, G. Bertoni, A. Cavalli, F. Scotognella, T. Pellegrino, L. Manna, *Chem. Mater.* **2016**, *28*, 4848.

[22] K. Ai, Y. Liu, J. Liu, Q. Yuan, Y. He, L. Lu, *Adv. Mater.* **2011**, *23*, 4886.

[23] G. Song, C. Liang, H. Gong, M. Li, X. Zheng, L. Cheng, K. Yang, X. Jiang, Z. Liu, *Adv. Mater.* **2015**, *27*, 6110.

[24] M. A. Hahn, A. K. Singh, P. Sharma, S. C. Brown, B. M. Moudgil, *Anal. Bioanal. Chem.* **2011**, *399*, 3.

[25] J. Mou, C. Liu, P. Li, Y. Chen, H. Xu, C. Wei, L. Song, J. Shi, H. Chen,

Biomaterials **2015**, *57*, 12.

[26] J. Y. Chang, J. M. Lin, L. F. Su, C. F. Chang, *ACS Appl. Mater. Interfaces* **2013**, *5*, 8740.

[27] J. Tang, Y. Ge, J. Shen, M. Ye, *Chem. Commun.* **2016**, *52*, 1509.

[28] K. Deng, Z. Hou, X. Deng, P. Yang, C. Li, J. Lin, *Adv. Funct. Mater.* **2015**, *25*, 7280.

[29] S. Wang, X. Li, Y. Chen, X. Cai, H. Yao, W. Gao, Y. Zheng, X. An, J. Shi, H. Chen, *Adv. Mater.* **2015**, *27*, 2775.

[30] W. H. De Jong, W. I. Hagens, P. Krystek, M. C. Burger, A. J. Sips, R. E. Geertsma, *Biomaterials* **2008**, *29*, 1912.

[31] G. Song, J. Hao, C. Liang, T. Liu, M. Gao, L. Cheng, J. Hu, Z. Liu, *Angew. Chem. Int. Edit.* **2016**, *55*, 2122.

[32] D. Santos-Carballal, A. Roldan, R. Grau-Crespo, N. H. de Leeuw, *Phys. Rev. B* **2015**, *91*, 195106.

[33] L. Y. Isseroff, E. A. Carter, *Phys. Rev. B* **2012**, *85*, 235142.

[34] B. Li, Y. Zhang, R. Zou, Q. Wang, B. Zhang, L. An, F. Yin, Y. Hua, J. Hu, *Dalton T.* **2014**, *43*, 6244.

[35] M. Zhou, M. Tian, C. Li, *Bioconjugate chem.* **2016**, *27*, 1188.

[36] E. Terreno, D. D. Castelli, A. Viale, S. Aime, *Chem. Rev.* **2010**, *110*, 3019.

[37] S. Viswanathan, Z. Kovacs, K. N. Green, S. J. Ratnakar, A. D. Sherry, *Chem. Rev.* **2010**, *110*, 2960.

[38] G. Kresse, J. Furthmüller, *Phys. Rev. B*, **1996**, *54*, 11169.

[39] J. P. Perdew, J. A. Chevary, S. H. Vosko, K. A. Jackson, M. R. Pederson, D. J. Singh, C. Fiolhais. *Phys. Rev. B* **1992**, *46*, 6671.

[40] K. Miyatani, T. Tanaka, S. Sakita, M. Ishikawa, N. Shirakawa, *Japan J. Appl. Phys.* **1993**, *32*.

[41] S.L. Dudarev, G.A. Botton, S.Y. Savrasov, C.J. Humphreys, A.P. Sutton, *Phys. Rev. B* **1998**, *57*, 1505.

[42] D.J. Chadi, M.L. Cohen, *Phys. Rev. B*, **1973**, *8*, 5747.

[43] H.J. Monkhorst, J.D. Pack, *Phys. Rev. B* **1976**, *13*, 5188.

The table of contents entry

Ultrasmall $CuCo_2S_4$ nanocrystals are developed as an efficient photothermal theragnosis agent. The nanocrystals exhibit intense near-infrared (NIR) absorption attributed to 3*d*-electronic transitions from the valence band (VB) to an intermediate band (IB), as identified by Density Functional Theory calculations, and capability for magnetic resonance (MR) imaging, as a result of the unpaired 3*d* electrons of cobalt.

Keywords: ternary bimetal chalcogenides, ultrasmall $CuCo_2S_4$ nanocrystals, DFT calculations, magnetic resonance imaging, photothermal therapy

By *Bo Li, Fukang Yuan, Guanjie He, Xiaoyu Han, Xin Wang, Jinbao Qin, Zheng Xiao Guo, Xinwu Lu,* Qian Wang, Ivan P. Parkin, Chengtie Wu**

Ultrasmall CuCo2S4 Nanocrystals: All-in-One Theragnosis Nanoplatform with Magnetic Resonance/Near-Infrared Imaging for Efficiently Photothermal Therapy of Tumors

ToC Figure

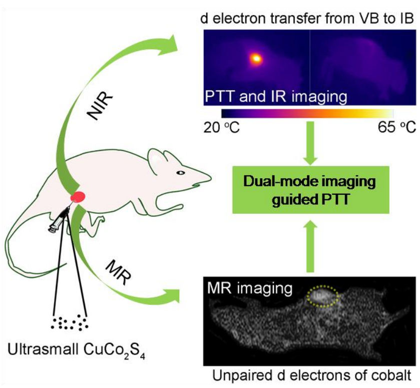

Click here to access/download
Production Data
Scheme 1.tif

Click here to access/download
Production Data
F1.tif

Click here to access/download
Production Data
F2.tif

Click here to access/download
Production Data
F3.tif

Click here to access/download
Production Data
F4.tif

Click here to access/download
Production Data
F5.tif

Click here to access/download
Production Data
F6.tif

Click here to access/download
Production Data
F7.tif